

Ferromagnetic and Half-Metallic FeC₂ Monolayer Containing C₂ Dimers

Tianshan Zhao,^{†,‡} Jian Zhou,[‡] Qian Wang,^{*,†,‡} Yoshiyuki Kawazoe,[§] and Puru Jena^{*,‡}

[†]Center for Applied Physics and Technology, College of Engineering, Peking University, Key Laboratory of High Energy Density Physics Simulation, and IFSA Collaborative Innovation Center, Ministry of Education, Beijing 100871, China

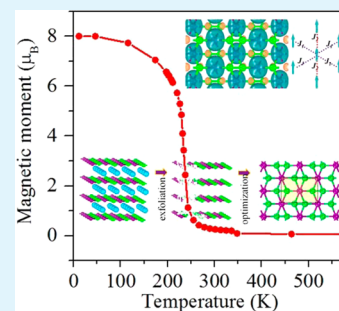
[‡]Department of Physics, Virginia Commonwealth University, Richmond, Virginia 23284, United States

[§]New Industry Creation Hatchery Center, Tohoku University, Sendai 980-8577, Japan

S Supporting Information

ABSTRACT: Ferromagnetism and half-metallicity are two vital properties of a material for realizing its potential in spintronics applications. However, none of the two-dimensional (2D) pristine metal–carbide sheets synthesized experimentally exhibits half-metallicity with ferromagnetic coupling. Here, a ferromagnetic and half-metallic FeC₂ sheet containing isolated C₂ dimers rather than individual carbon atoms is predicted to be such a material. Based on state-of-the-art theoretical calculations, we show that the FeC₂ sheet is dynamically, thermally, and mechanically stable and can be chemically exfoliated from the bulk phase of layered ThFeC₂. Due to its unique atomic configuration, the FeC₂ sheet exhibits ferromagnetism with a Curie temperature of 245 K. This is in contrast to its bulk counterpart, ThFeC₂, which is paramagnetic. We also find that, unlike the metallic metal–carbide sheets, the FeC₂ sheet is half-metallic with semiconducting spin-up and metallic spin-down channels. Moreover, half-metallicity can remain until an equi-biaxial strain of 10%. In addition, we provide the Raman and infrared spectra which can be used to identify this new 2D structure experimentally in the future.

KEYWORDS: ferromagnetism, half-metallicity, FeC₂ monolayer, C₂ dimer, electronic structure



INTRODUCTION

Bulk transition metal carbides constitute a diverse class of materials with many technological applications ranging from cutting tools, wear parts, optical coatings, and electrical contacts to diffusion barriers.^{1,2} In recent years, considerable attention has been paid to two-dimensional (2D) transition metal carbides, owing to their exceptional properties. One of these is the hotly pursued MXene type M_{n+1}C_n layers,³ where M is an early transition metal element including Ti, Sc, V, Cr, Zr, Nb, Mo, Hf, and Ta. Because of their rich chemistry, unique morphology, and good electronic conductivity, these 2D M_{n+1}C_n materials have vast potential for applications in sensors, electronic devices, catalysts, and so on.^{4,5} However, in MXenes, the atomic ratio of metal atoms is higher than that of carbon. Consequently, a high concentration of exposed metal sites makes such sheets less biocompatible and chemically less stable. In addition, all the synthesized pristine carbon containing MXenes are metallic and nonmagnetic,⁶ which limits their applications in spintronics. Thus, surface modification is usually needed for their practical application. To overcome these drawbacks, a TiC₂ sheet was recently proposed,⁷ which contains C₂ dimers^{8–10} instead of individual C atoms, resulting in less exposed metal sites on the surface. This leads to improved chemical stability, low mass density, high heat capacity, large Debye stiffness, and outstanding Li storage capacity with a small migration energy barrier.⁷ These novel

properties render the C₂ dimers containing sheet very appealing for many applications. However, the reported TiC₂ sheet is still metallic and nonmagnetic. How to synthesize such transition metal carbide sheets containing C₂ dimers remains unanswered from previous studies.⁷ Here we report a half-metallic and ferromagnetic 2D sheet composed of iron atoms and C₂ dimers and propose a possible way to synthesize it by chemical exfoliation from its parent three-dimensional (3D) ThFeC₂ crystal. This is possible because the structure of bulk ThFeC₂ consists of C₂ dimers bonded with Fe and Th atoms^{11,12} and is alternatively stacked between FeC₂ layers and Th atoms. Note that MXene monolayers have been chemically exfoliated from the MAX phases³ which belong to a family of transition metal carbides or nitrides. In this work, using first-principles calculations and molecular dynamics (MD) simulations based on density functional theory, we show that the FeC₂ sheet can be chemically exfoliated from bulk ThFeC₂. According to our phonon dispersion calculations, MD simulation, and mechanical parameters calculation, we show that FeC₂ sheet is dynamically, thermally, and mechanically stable. Different from the bulk phase of ThFeC₂ that is metallic and

Received: June 20, 2016

Accepted: September 13, 2016

Published: September 13, 2016

paramagnetic, the FeC₂ sheet is half-metallic and ferromagnetic with a Curie temperature (T_c) of 245 K.

METHODS

Our first-principles calculations are based on density functional theory (DFT) and the projector augmented wave (PAW) method¹³ as implemented in the Vienna *ab initio* Simulation Package (VASP).¹⁴ The electronic exchange-correlation interaction is treated using Perdew–Burke–Ernzerhof functional (PBE) within the generalized gradient approximation (GGA).¹⁵ The $2s^22p^2$, $3d^74s^1$, and $6s^26p^66d^27s^2$ atomic orbitals are treated as valence states for C, Fe, and Th, respectively. Plane waves with kinetic energy cutoff of 500 eV are used to expand the valence electron wave functions. To account for strong correlation of the unfilled d orbitals of Fe d and Th d atoms, we apply the GGA+U scheme.¹⁶ We carried out test calculations with effective U values ranging from 2 to a 6 eV, and adopted an effective U value of 5 eV for both Fe 3d and Th d orbitals in our calculations, in keeping with previous studies.^{17–21} Full geometry optimization without any symmetry constraint is carried out by using convergence criteria of 10^{-4} eV for total energy and 10^{-2} eV/Å for force component. We apply periodic boundary conditions with a vacuum space of 18 Å in order to avoid interactions between the layers in the nearest-neighbor unit cells. Since both bulk ThFeC₂ compound and the FeC₂ sheet are chemically bonded structures, the van der Waals (vdW) interaction corrections are not included. The first Brillouin zone is represented with a $9 \times 9 \times 1$ and $5 \times 7 \times 5$ Monkhorst–Pack special k -point mesh²² for the FeC₂ sheet and ThFeC₂ crystal, respectively. To confirm the dynamic stability, phonon calculations are performed using the phonopy program.²³ Thermal stability is studied using *ab initio* molecular dynamics (AIMD) simulations with temperature controlled by a Nosé heat bath scheme.²⁴

RESULTS AND DISCUSSION

Geometry. We begin our study by examining the bulk phase of ThFeC₂.^{11,12} The geometrical structure is shown in Figure 1a. The bulk phase is composed of two kinds of layers,

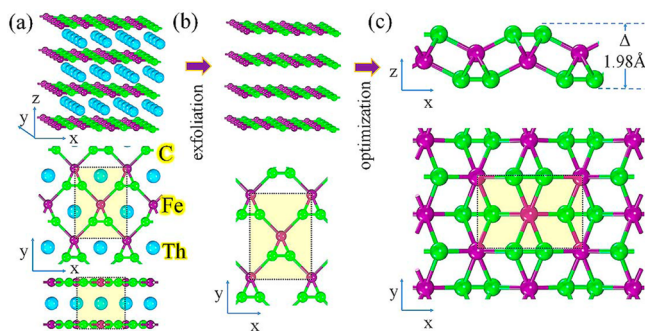


Figure 1. (a) Bulk phase of ThFeC₂. (b) FeC₂ layers exfoliated from bulk ThFeC₂. (c) Side and top views of the optimized FeC₂ sheet.

namely, the FeC₂ and Th atomic layers, which are alternatively stacked in the z -direction of the 3D crystal. It is well-known that, for van der Waals coupled layered structures such as graphite, mechanical exfoliation is sufficient to obtain the monolayer sheets, while, for chemically bonded layered bulk phases such as the MAX phases, chemical exfoliation technique has been developed to extract a single layer (MXene).³ Hence, the FeC₂ layers could be chemically exfoliated from the bulk phase of ThFeC₂, similar to exfoliating a MXene single layer from the MAX phase. The geometry of a FeC₂ layer directly exfoliated from the bulk phase is given in Figure 1b, which belongs to $Amm2$ space group where each Fe atom is 4-fold-coordinated with three C₂ dimers. After geometry relaxation,

the crystallographic symmetry of the sheet reduces to $Pm\bar{m}n$, where each Fe atom is 6-fold-coordinated and each carbon is 4-fold-coordinated, as shown in Figure 1c, exhibiting the characteristics of imperfect sp^3 hybridization,²⁵ similar to the case of the ThFeC₂ bulk phase^{12,26} and iron carbide clusters.²⁷ The optimized lattice parameters are $a = 4.535$ Å and $b = 2.887$ Å, and each unit cell contains two Fe and four C atoms. In this 2D structure, the FeC₂ sheet consists of three atomic layers with the Fe atoms in the middle and the C₂ dimers on the top and bottom layers. The total “thickness” Δ is 1.980 Å, as shown in Figure 1c. The optimized Fe–C bond length is 1.84 (2.11) Å along the x (y)-direction. The bond length of the C₂ dimer is 1.33 Å, which is comparable with 1.32–1.47 Å in the ThFeC₂ bulk phase^{12,26} and is the same as that in the FeC₂ gas phase molecule.²⁸ The coordinates are given in the Supporting Information (SI). We estimate the exfoliation energy E_{ex} , which is defined as the energy required to exfoliate one FeC₂ layer from a ThFeC₂ surface. In our calculation, the ThFeC₂ surface is represented by a five layered ThFeC₂ slab, with the coordinates of atoms in the bottom two layers fixed during the geometry relaxation. E_{ex} can then be expressed as

$$E_{\text{ex}} = E_{\text{FeC}_2} + E_{(\text{ThFeC}_2)_4 + \text{Th}} - E_{(\text{ThFeC}_2)_5}$$

With all the geometries in this equation fully optimized, we obtain $E_{\text{ex}} = 1.91 \times 10^{-4}$ J/cm². We also calculate the formation energy^{29,30} of the FeC₂ sheet, which is defined as $E_f = (E_{\text{FeC}_2} - 2\mu_C - \mu_{\text{Fe}})/3$, where E_{FeC_2} is the total energy per formula unit, and μ_C and μ_{Fe} are chemical potentials of graphene and bcc-Fe, respectively. The calculated formation energy is -0.23 eV/atom. The negative value corresponds to an exothermic reaction, which further confirms its stability.

Dynamical Stability. To confirm the dynamical stability of the FeC₂ sheet, we first calculate its phonon dispersion. The results are plotted in Figure 2a, which shows that the FeC₂ sheet is dynamically stable because all the vibrational modes are real in the whole Brillouin zone. The vibrational modes below 350 cm⁻¹ consist of three acoustic bands and three optical bands, which are mainly contributed by the Fe atoms due to its greater atomic number. The two highest optical vibrational

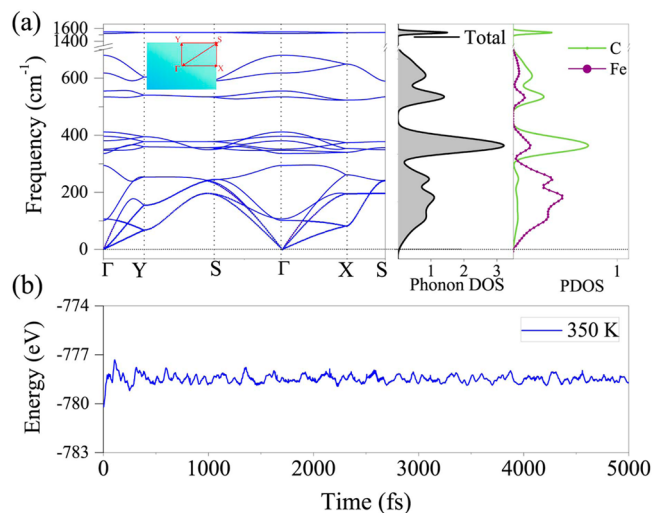


Figure 2. (a) Phonon band structures, total phonon DOS, and partial DOS. (b) Total potential energy fluctuation during AIMD simulations at 350 K of the FeC₂ sheet.

modes are separated from other optical vibrational modes by a large phonon gap of around 800 cm^{-1} .

Thermal Stability. We next examine its thermal stability by performing AIMD simulations. A $4 \times 4 \times 1$ supercell containing 96 atoms is used to reduce lattice translational constraints. The simulations are carried out with a Nosé–Hoover heat bath scheme²⁴ at 350 K for 5 ps with a time step of 1 fs. This simulation time is consistent with what has been used in previous works.^{31,32} The fluctuation of total potential energy with simulation time is shown in Figure 2b. After simulation, we find that the average value of the total potential energy remains nearly constant during the entire simulation, confirming that this new sheet is stable at room temperature.

Mechanical Stability. To further confirm the mechanical stability of the FeC_2 sheet based on Born criteria,^{33,34} we calculate its elastic constants. In the linear elastic range, the elastic constant tensor forms a symmetric 6×6 matrix with 21 independent components.^{35,36} The elastic constants are calculated to be $C_{11} = 133.29\text{ N/m}$, $C_{22} = 68.18\text{ N/m}$, $C_{12} = 24.80\text{ N/m}$, and $C_{44} = 15.19\text{ N/m}$. These values comply with the Born criteria,^{33,34} namely, $C_{11}, C_{22}, C_{44} > 0$ and $C_{11}C_{22} - C_{12}^2 > 0$, demonstrating that the FeC_2 sheet is mechanically stable.

Mechanical Properties. Having confirmed the stability of the FeC_2 sheet, we study its mechanical properties. The in-plane Young's modulus, calculated by using $E = (C_{11}^2 - C_{12}^2)/C_{11}$, is $98.41\text{ GPa}\cdot\text{nm}$, which is much smaller than that of graphene ($345\text{ GPa}\cdot\text{nm}$).³⁷ The Poisson ratio, calculated using $\nu_{12} = \nu_{21} = C_{12}/C_{11}$, is 0.186. In addition, we find that the phonon softening does not happen until 21% equi-biaxial tensile strain, as shown in Figure S1. We note that the magnitude of the strain the FeC_2 sheet can withstand is larger than the 14.8% of graphene³⁸ and 17.1% of penta-graphene,³² confirming its ultrahigh ideal strength. At the critical strained state, the Fe–C bond length in the x (y)-direction increases to 2.13 (2.21) Å from 1.839 (2.105) Å, while the C–C bond length decreases to 1.31 Å from 1.33 Å; see Figure S2 for details.

Magnetic Coupling and Electronic Properties. We next study the magnetic coupling between the Fe atoms in the FeC_2 sheet by calculating the total energies of the ferromagnetic (FM) and antiferromagnetic (AFM) configurations in the unit cell, and the AFM and ferrimagnetic (FIM) configurations in a 1×2 supercell, as shown in Figure 3. The FM configurations shown in Figure 3a are found to be 64, 68, and 112 meV lower in energy than the AFM_1 , AFM_2 , and FIM ones per unit cell, respectively, indicating that the Fe atoms prefer to couple ferromagnetically in the FeC_2 sheet. The total magnetic moment per unit cell is found to be $8.00\ \mu_B$, which is mostly located on and equally shared by the two Fe atoms; *i.e.*, each Fe atom carries a magnetic moment of $\sim 4.00\ \mu_B$. For comparison, calculations are also carried out for bulk ThFeC_2 , which is paramagnetic. The details are given in SI Figure S3.

To further understand the magnetic and electronic properties, we calculate the band structure of the FeC_2 sheet. The band dispersion shows very different conductivity in the spin-up and spin-down channels. The spin-up channel shows a semiconducting feature with a large quasi-direct band gap of 3.21 eV, while the spin-down channel is metallic, as the partially occupied bands cross the Fermi level in the vicinity of the Γ and S points in the Brillouin zone (see Figure 4a). Therefore, the FeC_2 sheet is half-metallic different with other 2D materials.^{29,31} Examination of the band decomposition near

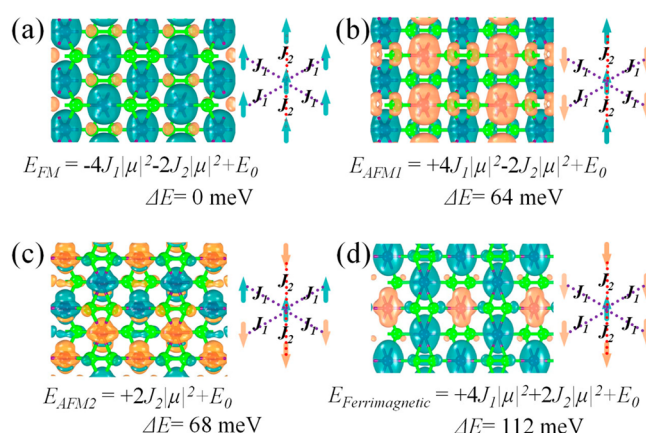


Figure 3. Spin density isosurface with a value of $0.1\text{ e}/\text{\AA}^3$ for the FM (a), AFM_1 (b), AFM_2 (c), and FIM (d) coupling configurations of the FeC_2 sheet. The relative energies ΔE calculated with respect to the lowest energy configuration (a) are also given.

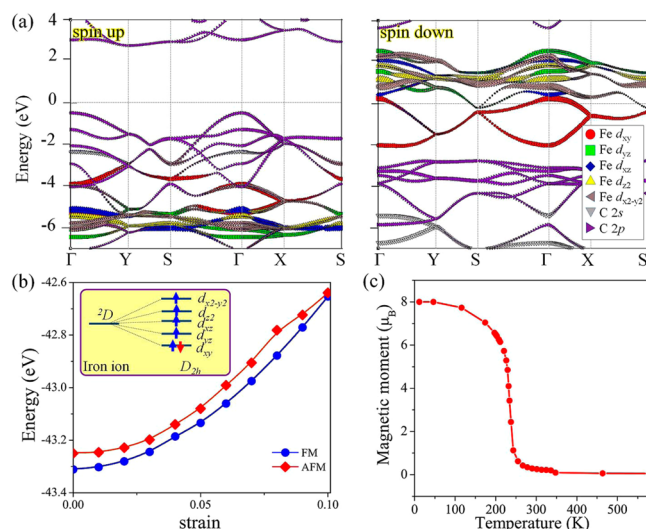


Figure 4. (a) Band structure of the FeC_2 sheet decomposed with respect to the Fe 3d, C 2s, and C 2p orbitals. (b) Variation of the total energy per unit cell of the FM and AFM configurations with the external strain. (Inset) Energy level diagram of Fe^{2+} ion in D_{2h} crystal field environment. (c) Variation of the total magnetic moment per unit cell of the FeC_2 sheet with temperature.

the Fermi level reveals that the Fe d_{xy} orbitals contribute to the valence band and the Fe d_{xz} , d_{yz} , and $d_{x^2-y^2}$ orbitals contribute to the two conduction bands crossing the Fermi level in the spin-down channel, as shown in Figure 4a. In the spin-up channel, the valence band maximum (VBM) and the conduction band minimum (CBM) are derived from the C 2p orbitals. The C_2 dimers with a large electronegativity receive electrons from the Fe atoms. Due to the presence of spin splitting, the same single particle orbital dispersions in the two channels lie at different energies. Hence hybridizations among the different orbitals (especially p–d hybridization) in each spin channel are also different, which makes the dispersions in the two spin channels different.

In order to explore the effect of spin–orbit coupling (SOC) on the band dispersion of the FeC_2 sheet, we perform band structure calculations at the PBE+U+SOC level. The band structures with and without SOC are plotted in Figure S4, for comparison. We observe that the band dispersions are nearly

maintained after SOC is included, and the metallic feature is unchanged. For comparison, the calculated band structure of the bulk ThFeC₂ is given in Figure S5. We note a metallic feature with the main contribution to metallicity coming from the Fe 3d orbitals. One can see that the FeC₂ sheet displays different electronic properties from the ThFeC₂ bulk phase: the 2D sheet is half-metallic, while the 3D bulk is metallic.

In the FeC₂ sheet, the Fe atom is in a high spin state, as the weak ligand effect of the C₂ dimer causes small crystal field splitting.²⁹ A quantitative analysis shows that the Fe atom has five d electrons occupying the spin-up d_{xy} , d_{xz} , d_{yz} , d_z^2 , and $d_{x^2-y^2}$ orbitals, and one d electron occupying the spin-down d_{xy} orbital, as shown in the inset of Figure 4b.

To confirm robustness of the magnetic stability, we calculate the variation of the total energies of the FM and AFM configurations (as shown in Figure 3a,b) with equi-biaxial strain increasing from 0% to 10%. Note although the ideal strength of the FeC₂ sheet is 20%, here we only consider equi-biaxial strain up to 10% because such high strain is very challenging to be achieved in experiments. The calculated results are plotted in Figure 4b. The FM coupling remains the preferred state, but the energy difference between the FM and AFM₁ configurations decreases. The variations of the bond lengths of Fe–Fe, C–C, and Fe–C with the equi-biaxial strain are given in Figure S2, respectively. The Fe–Fe bond length increases to 3.035 Å under 10% equi-biaxial strain. The Fe–C bond lengths in the *x*- and *y*-directions increase to 1.960 and 2.171 Å, respectively, while the C–C bond length decreases to 2.172 Å.

Curie Temperature. In order to estimate the Curie temperature (T_c) of the FeC₂ sheet, we use Monte Carlo (MC) simulation based on a simplified Ising model, $E_{\text{ex}} = -\sum_{ij} J_{ij}\mu_i\mu_j$, where μ_i (μ_j) indicates the magnetic moment of site *i* (site *j*), and J_{ij} is the magnetic exchange parameter between *i* and *j*. As shown in Figure 3a–c, we take into account two types of interactions in the Ising model, namely, type I (with exchange parameter J_1) and type II (with exchange parameter J_2). In order to estimate J_1 and J_2 , we use DFT to calculate the total energy for each coupling configuration as shown in Figure 3a–c. The total energy of each magnetic state is written as $E = E_0 + E_{\text{ex}}$, where E_0 is the total energy excluding the magnetic coupling (not sensitive to different magnetic states). Thus, the exchange parameters can be derived as

$$J_1 = -(E_{\text{FM}} - E_{\text{AFM}_1})/8\mu^2 \quad (1)$$

$$J_2 = -(E_{\text{FM}} + E_{\text{AFM}_1} - 2E_{\text{AFM}_2})/8\mu^2 \quad (2)$$

The exchange parameters J_1 and J_2 are estimated to be 0.50 and 0.56 meV, respectively. In the MC simulation, we use a 50 × 50 supercell to reduce the periodic constraints. At each temperature, 5 × 10⁹ steps are taken to achieve the equilibrated magnetic moment. The variation of the magnetic moment per unit cell with temperature is plotted in Figure 4c. T_c is estimated to be about 245 K, which is two times larger than

$$\Gamma = 3A_g(\text{R}) \oplus B_{1g}(\text{R}) \oplus 3B_{2g}(\text{R}) \oplus 2B_{3g}(\text{R}) \oplus A_u \oplus 3B_{1u}(\text{I}) \oplus 2B_{2u}(\text{I}) \oplus 3B_{3u}(\text{I}) \quad (3)$$

Here A_g , B_{1g} , B_{2g} , and B_{3g} are Raman-active, B_{1u} , B_{2u} , and B_{3u} are infrared-active, and A_u is neither Raman-active nor infrared-active. The calculated Raman and IR vibrational modes with corresponding wave numbers are presented in Figure 5a. The vibrational modes with corresponding wave numbers for the

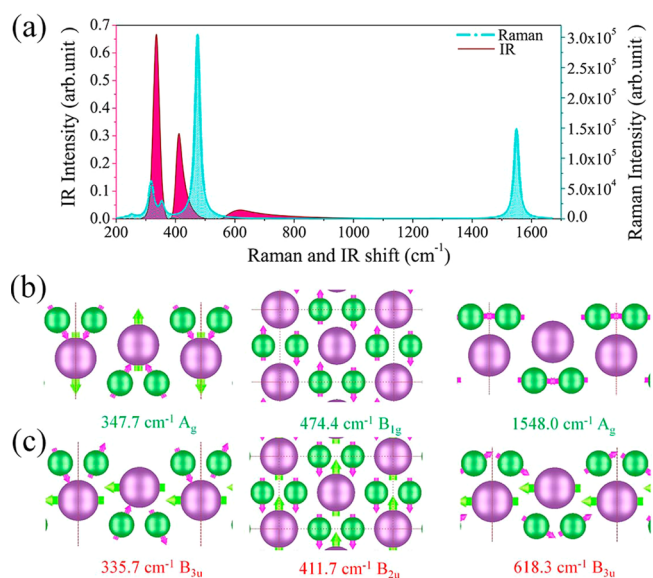


Figure 5. (a) Raman and IR spectra. (b) Three Raman modes corresponding to the three intensity peaks. (c) Three IR modes corresponding to the three intensity peaks. Arrows represent the directions of oscillation.

that of 2D MnO₂³⁹ and shows better spin half-metallic property than AFM 2D MoS₂.⁴⁰

Since Fe and C belong to 3d and 2p blocks in the periodic table, respectively, their SOC coefficients are small (proportional to Z^4 , where Z is the atomic number). We thus calculate the magnetocrystalline anisotropy energy (MAE) including SOC interactions.⁴¹ We find that the easy axis is along the *z*-direction (out-of-plane), and the magnetization along the *z*-direction is lower in energy than that along the *x*- and *y*-directions by 1.67 and 0.98 meV per unit cell, respectively. Since the MAE value is small, use of the Heisenberg model that includes the quantum fluctuation and magnetocrystalline anisotropy would lower the estimated Curie temperature. However, previous studies on FM (La_{0.75}Ca_{0.25})(Mn_{0.5}Zn_{0.5})AsO and La(Mn_{0.5}Zn_{0.5})As(O_{0.5}H_{0.5}) show that the estimated T_c based on the Heisenberg model is comparable with those using the Ising model.⁴² Thus, in the current study we used the Ising model to facilitate comparison with previous theoretical studies^{39,43} which estimated T_c of 2D ferromagnetic materials by using the nearest-neighbor Ising model.

Raman and IR Spectra. Based on phonon vibrational properties at the Γ point in the Brillouin zone center, we simulate the Raman and IR spectra of the FeC₂ sheet, which are related to the symmetry of the structure. We note that the little group of the Γ point is D_{2h} , which has eight one-dimensional irreducible representations at the Brillouin zone center and can be expressed as

intense peaks shown in Figure 5a are plotted in Figure 5b,c, which show that the out-of-plane vibration of C dimers and Fe atoms leads to the Raman A_g active mode at 347.7 cm⁻¹, the out-of-plane vibration of the C dimers and in-plane Fe atoms lead to the Raman B_{2g} active mode at 474.4 cm⁻¹, and the

vibration mode of the C=C bond is at 1548.0 cm^{-1} , which was also observed in other materials containing C_2 dimers.^{44,45} The three IR modes are at 335.7 , 411.7 , and 618.3 cm^{-1} , respectively. The nine Raman-active and eight IR-possible modes are given in Figure S6. To analyze Raman- and IR-active modes, the variation of dipole moments are given by using group theory in Figure Sb (see SI section for details). The FeC_2 Raman simulated spectrum covers a large range from 200 to 600 cm^{-1} and from 1450 to 1650 cm^{-1} , and the distribution of the IR spectrum is from 200 to 800 cm^{-1} , as shown in Figure 5a. The simulated Raman and IR spectra of the FeC_2 sheet would be useful to experimentally identify the 2D crystal structure in the future.

SUMMARY

Unlike C atoms, C_2 is a well-known pseudohalogen with an electron affinity of 3.4 eV and is an important structural unit in bulk transition metal carbides. In this study, we report, for the first time, a new FeC_2 sheet containing C_2 dimers, which can be chemically exfoliated from bulk ThFeC_2 phase. Using density functional theory combined with AIMD and phonon dispersion calculation, we found that, upon exfoliation from bulk ThFeC_2 , the FeC_2 sheet changes its symmetry from $Amm2$ to $Pmmn$, while retaining its robust dynamical, thermal, and mechanical stability. In sharp contrast to the metallic and paramagnetic bulk phase of ThFeC_2 and the recently reported TiC_2 sheet, the exfoliated FeC_2 sheet is half-metallic and ferromagnetic with a Curie temperature of 245 K , making it a promising candidate for spintronic applications. In addition, the FeC_2 sheet has an ultrahigh ideal strength, nine Raman-active modes with a strong intensity at 474.4 cm^{-1} and eight IR modes with strong intensity at 335.7 cm^{-1} . We hope that the present theoretical study will stimulate experimental exploration of transition metal carbide sheets containing C_2 dimers, which are beyond the conventional MXenes and have many potential applications.

ASSOCIATED CONTENT

Supporting Information

The Supporting Information is available free of charge on the ACS Publications website at DOI: [10.1021/acsami.6b07482](https://doi.org/10.1021/acsami.6b07482).

Phonon bands at the extreme equi-biaxial strain, variation of the bond lengths with the strain of the FeC_2 sheet, spin density isosurfaces for different magnetic coupling configurations, electronic band structures of bulk ThFeC_2 , zone center vibrational modes of the FeC_2 sheet, and optimized lattice constants and geometric coordinates of the FeC_2 sheet (PDF)

AUTHOR INFORMATION

Corresponding Authors

*(Q.W.) E-mail: qianwang2@pku.edu.cn.

*(P.J.) E-mail: pjena@vcu.edu.

Notes

The authors declare no competing financial interest.

ACKNOWLEDGMENTS

This work is partially supported by grants from the National Natural Science Foundation of China (Grant NSFC-51471004), the National Grand Fundamental Research 973 Program of China (Grant 2012CB921404), and the Doctoral Program of Higher Education of China (Grant 20130001110033). P.J. acknowledges support by the U.S.

Department of Energy, Office of Basic Energy Sciences, Division of Materials Sciences and Engineering under Award No. DE-FG02-96ER45579. T.Z. acknowledges the China Scholarship Council (CSC) for sponsoring his visit to Virginia Commonwealth University (VCU). We thank the crew of the Center for Computational Materials Science, the Institute for Materials Research, Tohoku University (Japan), for their continuous support of the HITACHI SR11000 supercomputing facility.

REFERENCES

- (1) Valade, L.; Choukroun, R.; Cassoux, P.; Teyssandier, F.; Poirier, L.; Ducarroir, M.; Feurer, R.; Bonnefond, P.; Maury, F. Single-Source Precursors for the Chemical Vapor Deposition of Titanium and Vanadium Carbide and Nitride. In *The Chemistry of Transition Metal Carbides and Nitrides*; Oyama, S. T., Ed.; Springer: Dordrecht, The Netherlands, 1996; pp 290–310, DOI: [10.1007/978-94-009-1565-7_15](https://doi.org/10.1007/978-94-009-1565-7_15).
- (2) Oyama, S. T. Introduction to the Chemistry of Transition Metal Carbides and Nitrides. In *The Chemistry of Transition Metal Carbides and Nitrides*; Oyama, S. T., Ed.; Springer: Dordrecht, The Netherlands, 1996; DOI: [10.1007/978-94-009-1565-7_1](https://doi.org/10.1007/978-94-009-1565-7_1).
- (3) Naguib, M.; Kurtoglu, M.; Presser, V.; Lu, J.; Niu, J.; Heon, M.; Hultman, L.; Gogotsi, Y.; Barsoum, M. W. Two-Dimensional Nanocrystals Produced by Exfoliation of Ti_3AlC_2 . *Adv. Mater.* **2011**, *23*, 4248–4253.
- (4) Naguib, M.; Mochalin, V. N.; Barsoum, M. W.; Gogotsi, Y. 25th Anniversary Article: MXenes: A New Family of Two-Dimensional Materials. *Adv. Mater.* **2014**, *26*, 992–1005.
- (5) Naguib, M.; Gogotsi, Y. Synthesis of Two-Dimensional Materials by Selective Extraction. *Acc. Chem. Res.* **2015**, *48*, 128–135.
- (6) Khazaei, M.; Arai, M.; Sasaki, T.; Chung, C.-Y.; Venkataraman, N. S.; Estili, M.; Sakka, Y.; Kawazoe, Y. Novel Electronic and Magnetic Properties of Two-Dimensional Transition Metal Carbides and Nitrides. *Adv. Funct. Mater.* **2013**, *23*, 2185–2192.
- (7) Zhao, T.; Zhang, S.; Guo, Y.; Wang, Q. TiC_2 : A New Two-Dimensional Sheet beyond MXenes. *Nanoscale* **2016**, *8*, 233–242.
- (8) Wang, L.-S.; Cheng, H. Growth Pathways of Metallo-carbohedrenes: Cagelike or Cubic? *Phys. Rev. Lett.* **1997**, *78*, 2983–2986.
- (9) Jena, P.; Castleman, A. W. *Introduction to Atomic Clusters* **2010**, *1*, 1–36.
- (10) Reddy, B. V.; Khanna, S. N.; Jena, P. Electronic, Magnetic, and Geometric Structure of Metallo-Carbohedrenes. *Science* **1992**, *258*, 1640–1643.
- (11) Li, J.; Hoffmann, R. How Carbon-Carbon Bonds are Formed and How They Influence Structural Choices in Some Binary and Ternary Metal Carbides. *Chem. Mater.* **1989**, *1*, 83–101.
- (12) Gerss, M. H.; Jeitschko, W. The Crystal Structures of Ternary Actinoid Iron (Cobalt, Nickel) Carbides with Composition 1:1:2. *Mater. Res. Bull.* **1986**, *21*, 209–216.
- (13) Gajdoš, M.; Hummer, K.; Kresse, G.; Furthmüller, J.; Bechstedt, F. Linear Optical Properties in the Projector-Augmented Wave Methodology. *Phys. Rev. B: Condens. Matter Mater. Phys.* **2006**, *73*, 045112.
- (14) Kresse, G.; Furthmüller, J. Efficient Iterative Schemes for Ab Initio Total-Energy Calculations Using a Plane-Wave Basis Set. *Phys. Rev. B: Condens. Matter Mater. Phys.* **1996**, *54*, 11169.
- (15) Perdew, J. P.; Burke, K.; Ernzerhof, M. Projector Augmented-Wave Method. *Phys. Rev. Lett.* **1996**, *77*, 3865.
- (16) Dudarev, S. L.; Botton, G. A.; Savrasov, S. Y.; Humphreys, C. J.; Sutton, A. P. Electron-Energy-Loss Spectra and the Structural Stability of Nickel Oxide: An LSDA+U Study. *Phys. Rev. B: Condens. Matter Mater. Phys.* **1998**, *57*, 1505–1509.
- (17) Anisimov, V. I.; Elfimov, I. S.; Hamada, N.; Terakura, K. Charge-Ordered Insulating State of Fe_3O_4 from First-Principles Electronic Structure Calculations. *Phys. Rev. B: Condens. Matter Mater. Phys.* **1996**, *54*, 4387–4390.

- (18) Pickett, W. E.; Erwin, S. C.; Ethridge, E. C. Reformulation of the LDA+U Method for a Local-Orbital Basis. *Phys. Rev. B: Condens. Matter Mater. Phys.* **1998**, *58*, 1201–1209.
- (19) Zhou, F.; Cococcioni, M.; Marianetti, C. A.; Morgan, D.; Ceder, G. First-Principles Prediction of Redox Potentials in Transition-Metal Compounds with LDA+U. *Phys. Rev. B: Condens. Matter Mater. Phys.* **2004**, *70*, 235121.
- (20) Pentcheva, R.; Nabi, H. S. Interface Magnetism in $\text{Fe}_2\text{O}_3\text{FeTiO}_3$ Heterostructures. *Phys. Rev. B: Condens. Matter Mater. Phys.* **2008**, *77*, 172405.
- (21) Sevik, C.; Çağın, T. Mechanical and Electronic Properties of CeO_2 , ThO_2 , and $(\text{Ce,Th})\text{O}_2$ Alloys. *Phys. Rev. B: Condens. Matter Mater. Phys.* **2009**, *80*, 014108.
- (22) Monkhorst, H. J.; Pack, J. D. Special Points for Brillouin-Zone Integrations. *Phys. Rev. B* **1976**, *13*, 5188–5192.
- (23) Togo, A.; Oba, F.; Tanaka, I. First-Principles Calculations of the Ferroelastic Transition between Rutile-Type and $\text{CaCl}_2\text{SiO}_2$ at High Pressures. *Phys. Rev. B: Condens. Matter Mater. Phys.* **2008**, *78*, 134106.
- (24) Nosé, S. A Unified Formulation of the Constant Temperature Molecular Dynamics Methods. *J. Chem. Phys.* **1984**, *81*, 511–519.
- (25) Grigorovici, R. Structure of Amorphous Semiconductors. In *Amorphous and Liquid Semiconductors*; Tauc, J., Ed.; Springer: Boston, MA, USA, 1974; pp 45–99, DOI: [10.1007/978-1-4615-8705-7_2](https://doi.org/10.1007/978-1-4615-8705-7_2).
- (26) Grant, T.; Machado, A. J. S.; Kim, D. J.; Fisk, Z. Superconductivity in Non-Centrosymmetric ThCoC_2 . *Supercond. Sci. Technol.* **2014**, *27*, 035004.
- (27) Pilgrim, J. S.; Duncan, M. A. Metallo-Carbohedrenes: Chromium, Iron, and Molybdenum Analogs. *J. Am. Chem. Soc.* **1993**, *115*, 6958–6961.
- (28) Noya, E. G.; Longo, R. C.; Gallego, L. J. Density-Functional Calculations of the Structures, Binding Energies, and Spin Multiplicities of Fe–C clusters. *J. Chem. Phys.* **2003**, *119*, 11130–11134.
- (29) Zheng, F.; Zhang, C. The Electronic and Magnetic Properties of Functionalized Silicene: A First-Principles Study. *Nanoscale Res. Lett.* **2012**, *7*, 422.
- (30) Zhang, R.-w.; Zhang, C.-w.; Ji, W.-x.; Li, S.-s.; Yan, S.-s.; Li, P.; Wang, P.-j. Functionalized Thallium Antimony Films as Excellent Candidates for Large-Gap Quantum Spin Hall Insulator. *Sci. Rep.* **2016**, *6*, 21351.
- (31) Zhang, C.-w.; Yan, S.-s. First-Principles Study of Ferromagnetism in Two-Dimensional Silicene with Hydrogenation. *J. Phys. Chem. C* **2012**, *116*, 4163–4166.
- (32) Zhang, S.; Zhou, J.; Wang, Q.; Chen, X.; Kawazoe, Y.; Jena, P. Penta-Graphene: A new Carbon Allotrope. *Proc. Natl. Acad. Sci. U. S. A.* **2015**, *112*, 2372–2377.
- (33) Born, M.; Huang, K. *Dynamical Theory of Crystal Lattices*; Clarendon: Oxford, U.K., 1954.
- (34) Wang, J.; Yip, S.; Phillpot, S. R.; Wolf, D. Crystal Instabilities at Finite Strain. *Phys. Rev. Lett.* **1993**, *71*, 4182–4185.
- (35) Cadelano, E.; Colombo, L. Effect of Hydrogen Coverage on the Young's Modulus of Graphene. *Phys. Rev. B: Condens. Matter Mater. Phys.* **2012**, *85*, 245434.
- (36) Cadelano, E.; Palla, P. L.; Giordano, S.; Colombo, L. Elastic Properties of Hydrogenated Graphene. *Phys. Rev. B: Condens. Matter Mater. Phys.* **2010**, *82*, 235414.
- (37) Lee, C.; Wei, X.; Kysar, J. W.; Hone, J. Measurement of the Elastic Properties and Intrinsic Strength of Monolayer Graphene. *Science* **2008**, *321*, 385–388.
- (38) Novoselov, K. S.; Geim, A. K.; Morozov, S. V.; Jiang, D.; Zhang, Y.; Dubonos, S. V.; Grigorieva, I. V.; Firsov, A. A. Electric Field Effect in Atomically Thin Carbon Films. *Science* **2004**, *306*, 666–669.
- (39) Kan, M.; Zhou, J.; Sun, Q.; Kawazoe, Y.; Jena, P. The Intrinsic Ferromagnetism in a MnO_2 Monolayer. *J. Phys. Chem. Lett.* **2013**, *4*, 3382–3386.
- (40) Kan, M.; Wang, J. Y.; Li, X. W.; Zhang, S. H.; Li, Y. W.; Kawazoe, Y.; Sun, Q.; Jena, P. Structures and Phase Transition of a MoS_2 Monolayer. *J. Phys. Chem. C* **2014**, *118*, 1515–1522.
- (41) Zhou, J.; Wang, Q.; Sun, Q.; Kawazoe, Y.; Jena, P. Giant Magnetocrystalline Anisotropy of 5d Transition Metal-Based Phthalocyanine Sheet. *Phys. Chem. Chem. Phys.* **2015**, *17*, 17182–17189.
- (42) Li, X.; Wu, X.; Yang, J. Room-Temperature Half-Metallicity in $\text{La}(\text{Mn,Zn})\text{AsO}$ Alloy via Element Substitutions. *J. Am. Chem. Soc.* **2014**, *136*, 5664–5669.
- (43) Wu, F.; Huang, C.; Wu, H.; Lee, C.; Deng, K.; Kan, E.; Jena, P. Atomically Thin Transition-Metal Dinitrides: High-Temperature Ferromagnetism and Half-Metallicity. *Nano Lett.* **2015**, *15*, 8277–8281.
- (44) Tan, P. H.; Han, W. P.; Zhao, W. J.; Wu, Z. H.; Chang, K.; Wang, H.; Wang, Y. F.; Bonini, N.; Marzari, N.; Pugno, N.; Savini, G.; Lombardo, A.; Ferrari, A. C. The Shear Mode of Multilayer Graphene. *Nat. Mater.* **2012**, *11*, 294–300.
- (45) Lui, C. H.; Ye, Z.; Keiser, C.; Xiao, X.; He, R. Temperature-Activated Layer-Breathing Vibrations in Few-Layer Graphene. *Nano Lett.* **2014**, *14*, 4615–4621.